ACS Photonics

Article

Cite This: ACS Photonics 2018, 5, 3331−3337

pubs.acs.org/journal/apchd5

Interminiband Optical Transitions in Graphene Lateral Superlattices

Yuyu Li and Roberto Paiella*

Department of Electrical and Computer Engineering and Photonics Center, Boston University, 8 Saint Mary's Street, Boston, Massachusetts 02215, United States

Supporting Information

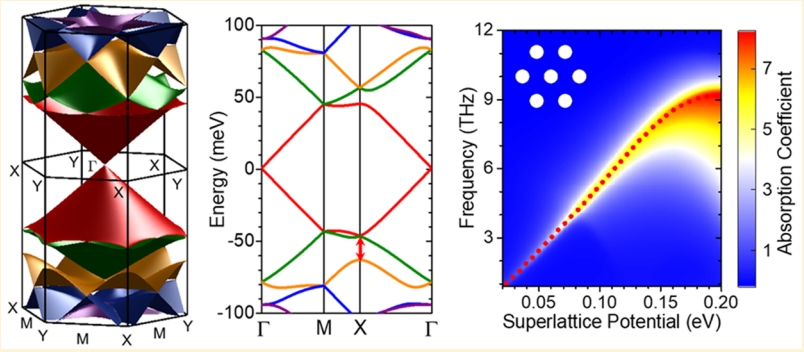

ABSTRACT: Gated graphene superlattices, where in-plane variations in the potential-energy profile are introduced with a periodic patterning of the gate electrode or dielectric, provide new opportunities for tailoring the electronic and optical properties of two-dimensional materials. Here we present a numerical study of the optical transitions between minibands derived from the same energy band (conduction or valence) in these systems. Giant absorption peaks at voltage-tunable THz frequencies are obtained, associated with van Hove singularities in the joint density of states of select pairs of minibands. Furthermore, we describe the possibility of interminiband THz gain in the same systems under external carrier injection, resulting from a local population inversion at specific symmetry points of the mini-Brillouin zone, even in the absence of a global inversion. These results highlight the great potential of engineered graphene superlattices for THz optoelectronic device applications, including modulators, tunable photodetectors, and lasers.

KEYWORDS: *graphene, terahertz photonics, superlattices, band structure engineering, optical absorption, optical gain*

Solid-state superlattices (SLs), where a periodic potential-energy profile is artificially superimposed on the lattice potential of a crystalline sample, have been studied extensively since the pioneering work of Esaki and Tsu in 1970.[1] These systems are most commonly implemented with vertically coupled semiconductor quantum wells, where the SL potential-energy profile is produced by the spatial variations of the conduction- and valence-band edges along the epitaxial growth direction. Over the past few decades, these structures have allowed for the investigation of a wide range of fundamental electronic phenomena, such as the opening of new energy bandgaps at the minizone boundaries, negative differential conductance, and Bloch oscillations.[2] Their optical properties have also been studied in detail, beginning with infrared absorption spectroscopy measurements.[3,4] Similar structures have then played a key role in the development of mid-infrared and THz quantum cascade lasers, including devices where stimulated emission involves electronic transitions between the first-excited and ground-state SL minibands at the minizone boundaries.[5−7]

More recently, renewed interest in SL material and device physics has focused on two-dimensional (2D) crystals, particularly graphene, in the presence of an external potential varying periodically on the sample plane. This lateral SL potential is obtained naturally in graphene transferred over hexagonal boron nitride (h-BN), when the orientations of the graphene and h-BN lattices are closely aligned.[8−13] Due to the lattice mismatch between the two crystals, a moiré pattern with suitably small periodicity (a few 10 nm) is then produced in their combined atomic arrangement, and as a result, the energy of the graphene carriers is modulated periodically by the nearby ionized B and N atoms. An alternative approach consists of introducing periodic variations in the graphene charge density (leading to a commensurate electrostatic potential-energy profile) via a suitable patterning of the chemical doping distribution,[14] gate electrode,[15,16] or gate dielectric.[17] The use of strain variations in graphene on a periodic array of supporting nanospheres has also been investigated recently.[18] Compared to moiré SLs, these engineered approaches generally feature more complex device geometries but, at the same time, offer greater design flexibility and, in the case of periodically gated samples, the possibility of dynamic tunability. Regardless of the physical origin of the

Received: May 4, 2018
Published: July 11, 2018

DOI: 10.1021/acsphotonics.8b00584
ACS Photonics 2018, 5, 3331−3337

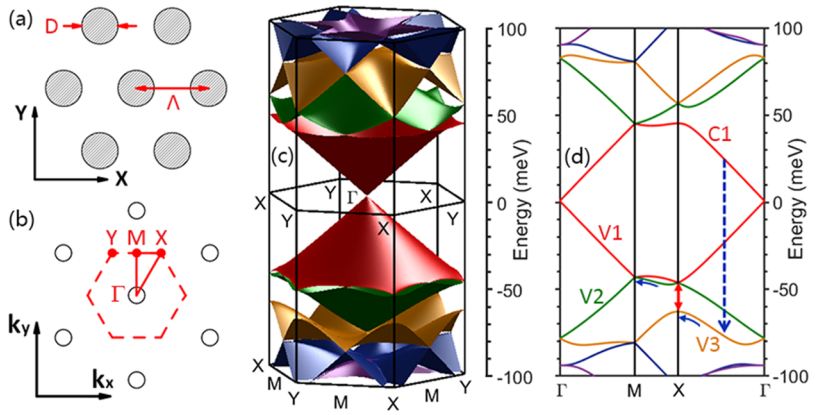

Figure 1. Periodically gated graphene SLs. (a) Schematic SL geometry. The circular regions are held at a constant electrostatic potential U_{SL} relative to the surrounding areas. (b) MBZ of the SL of (a). (c) Miniband structure of the same SL for Λ = 50 nm, $D = \Lambda/2$, and U_{SL} = 73 meV. (d) Dispersion of the minibands of (c) along selected symmetry lines of the MBZ. The solid double arrow indicates the interminiband transitions under study in this work. The dashed vertical arrow denotes the excitation of holes in miniband V3 at the pump-light photon energy used in the gain calculations of Figure 4. The curved arrows illustrate intraminiband hole relaxation processes in minibands V2 and V3.

periodic potential, the graphene band structure is strongly modified through the formation of minibands featuring new Dirac points on a mini-Brillouin zone (MBZ) determined by the SL symmetry and periodicity.[19−22] The resulting electronic properties have been studied in detail through extensive transport measurements, including the observation of fractal band structures under large magnetic fields[9−11,17] and ballistic miniband conduction.[13] The optical excitation of electron−hole pairs in moiré SLs has also been investigated via absorption spectroscopy[23] and photocurrent measurements.[24]

In this work, we present a numerical study of the optical transitions between minibands derived from the same energy band (conduction or valence) in graphene SLs. While these transitions form the basis of the most significant technological application of semiconductor SLs to date (quantum cascade lasers), they have so far remained largely unexplored in the context of 2D materials. Recent theoretical studies have shown the presence of sharp peaks in the THz conductivity of moiré-patterned graphene, associated with resonances across the lowest two valence minibands.[25,26] Here, we consider instead SLs based on periodic in-plane variations of the gate potential and investigate the dynamic tunability of their THz interminiband absorption spectra. Furthermore, we describe the feasibility of THz amplification in the same structures and compute their gain spectra based on a simple model of interminiband carrier dynamics. Our simulation results underscore the potential of engineered graphene SLs for the development of highly integrated and widely tunable THz devices, including modulators, photodetectors, and light emitters. It should be noted that graphene in general is already being widely investigated as a promising THz optoelectronic material, by virtue of its gapless and linear energy dispersion, record high room-temperature mobilities, and strongly confined far-infrared plasmonic excitations. Several innovative device concepts leveraging these distinctive properties have already been proposed and/or demonstrated for different applications.[27−43] While graphene SLs have not yet been considered in this context, the present work indicates that they may also play a particularly significant role for future THz device development.

PERIODICALLY GATED GRAPHENE SUPERLATTICES

The SL geometry under study consists of a single graphene layer (possibly encapsulated in h-BN for enhanced mobility[44]) featuring a triangular periodic array of circular regions where the electrostatic potential is held at a constant value U_{SL} relative to the remaining area of the sample (Figure 1a). This arrangement can be obtained in a double-gated graphene field-effect transistor, by introducing the same periodic variations in either top or bottom gate potential (with the other gate used to independently control the graphene Fermi level). Specific device structures could be implemented with a periodic patterning of the top gate contact[15,16] or by introducing a commensurate lattice of air holes in the bottom gate dielectric.[17] In passing, we note that similar structures (albeit with larger periods) have also been developed recently for the study of THz plasmon polaritons in graphene.[45,46] In the following we present simulation results for a constant array period Λ = 50 nm, which is well below the collision mean free path of carriers in high-quality graphene samples, and at the same time large enough to be accessible with current nanofabrication techniques. The diameter D of the circular regions is fixed at $\Lambda/2$.

The SL miniband structure is computed by diagonalizing the electronic effective Hamiltonian near the Dirac points, including the SL periodic potential, in the basis of the energy eigenstates of graphene in the absence of any external perturbation.[19] The absorption spectrum can then be evaluated from the dynamic conductivity using the approach described, for example, in ref 47, which, when applied to a graphene SL, produces the following expression

$$\alpha(\omega) = \frac{q^2 v_F^2}{\epsilon_0 c \omega} \mathrm{Im}\left[\frac{4}{A}\sum_{\mathbf{k}}\sum_{m,n\neq m} |\langle \psi_{m,\mathbf{k}}|\sigma_x|\psi_{n,\mathbf{k}}\rangle|^2 \times \frac{f(E_n(\mathbf{k})) - f(E_m(\mathbf{k}))}{\hbar(\omega + i\delta) - [E_m(\mathbf{k}) - E_n(\mathbf{k})]}\right] \quad (1)$$

Here α is the dimensionless absorption coefficient normalized to the inverse thickness of a graphene single layer; the incident light is assumed to be a harmonic plane wave of angular frequency ω and linear polarization along the x direction;

DOI: 10.1021/acsphotonics.8b00584
ACS Photonics 2018, 5, 3331−3337

$E_n(\mathbf{k})$ and $\psi_{n,\mathbf{k}}$ are the electronic energy eigenvalues and eigenvectors as a function of crystal wavevector $\mathbf{k}$ and miniband index n; the $\mathbf{k}$ sum is over the entire MBZ (shown schematically in Figure 1b); the indexes m and n in the second sum run over all SL minibands (both conduction and valence); $v_F \approx 1 \times 10^6$ m/s is the graphene Fermi velocity, A is the sample area, σ_x is the x component of the Pauli matrices, f is the electronic occupation probability, and $\tau_{sc} = \delta^{-1}$ is the scattering lifetime. The latter parameter is taken to be 1 ps, corresponding to a carrier mean free path $l = v_F\tau_{sc}$ of about 1 μm, which can be readily achieved even at room temperature in high-quality graphene samples fully encapsulated in h-BN,[44] even in the presence of an external SL potential.[17]

Figure 1c,d shows the calculated electronic band structure near the K Dirac point of plain graphene (relabeled Γ in these plots), for the device geometry of Figure 1a with U_{SL} = 73 meV. As expected in the presence of the periodic SL potential, both valence and conduction bands evolve into a series of minibands, labeled Vn and Cn in the following (where the positive integer n increases with increasing energy separation from the Dirac point). Importantly, any two consecutive minibands in these plots are connected to each other at least at one symmetry point of the MBZ, so that no full minigap is opened (as would be the case in a standard 2D electron gas under similar periodic potentials). This behavior is a consequence of the chiral nature of the graphene carriers, combined with the inversion and time-reversal symmetry of their Hamiltonian,[19] which is preserved even in the presence of the periodic potential of Figure 1a. (In contrast, full minigaps can be opened in graphene/h-BN moiré SLs, where the inversion symmetry of the graphene unit cell is broken by the different potentials of the nearby B and N atoms.[11]) In any case, pronounced local minigaps between consecutive minibands are still observed in Figure 1c,d at or near other symmetry points of the MBZ. The miniband structure shown in these figures also features a clear electron−hole asymmetry, which is related to the polarity of the SL voltage and thus can be reversed by changing the sign of U_{SL}.

INTERMINIBAND ABSORPTION

Depending on the carrier distribution among the different minibands, large resonant peaks in the SL absorption spectrum can be obtained, associated with van Hove singularities in the interminiband joint density of states. Here we focus on the local minigap between the second and third valence minibands at the X points of the MBZ (indicated by the solid double arrow in Figure 1d). This minigap occurs between the maximum of the miniband below and a local maximum (with a nearby saddle point) of the miniband above, and as a result can produce a particularly strong peak in the joint density of states, and thus in the interminiband absorption spectrum. This expectation is confirmed by the simulation results of Figure 2, where the absorption coefficient α of eq 1 is computed under conditions of thermal equilibrium at different temperatures T. The graphene Fermi energy E_F in these calculations is fixed at the bottom of the minigap under consideration, so as to maximize the electronic population difference between minibands V3 and V2 near the X point. A sharp absorption peak at the minigap frequency of 3.7 THz is obtained, with maximum value at low temperature as large as 4.7. This value is quite remarkable, considering the ultrasmall thickness of single-layer graphene. The corresponding single-pass absorbance (without accounting for reflection at the SL surface) is $1 - e^{-\alpha} = 99.1\%$, as opposed to 2.3% for the case of interband transitions in plain graphene.[47] As the temperature is increased, the peak absorbance decreases due to the thermal excitation of electrons across the V2−V3 minigap, but a large value above 60% is still computed at room temperature. Relatively strong and sharp absorption peaks are also computed for the same SL geometry with shorter scattering lifetimes τ_{sc} on the order of a few hundred fs (see Supporting Information, Figure S1). In passing, we note that eq 1 does not include the effect of free-carrier absorption, which however can be expected to be quite small at the low carrier density of the sample under study (3.3×10^{11} cm^{-2}). For example, using the Drude formula for the free-carrier absorption coefficient of plain graphene,[48] we find a negligible contribution of α_{FCA} = 0.006 at the peak absorption frequency of Figure 2.

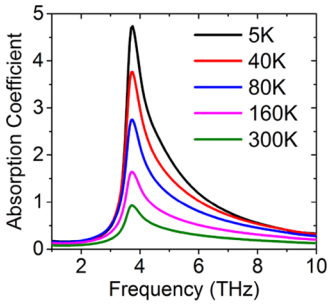

Figure 2. Interminiband absorption in graphene SLs. Absorption spectrum of the SL of Figure 1 under conditions of thermal equilibrium at different temperatures, with Fermi level at the top of miniband V3.

The absorption peak just described can also be tuned dynamically by varying the SL potential U_{SL} (Figure 3a), due to the resulting variations in the SL miniband structure. In particular, the energy separation between minibands V2 and V3 increases with increasing U_{SL}, while at the same time their curvatures near the X point decrease (Figure 3b), leading to a proportional enhancement in their joint density of states. As a result, the absorption peak is blue-shifted, and simultaneously increased and broadened. This behavior is illustrated in the color map of Figure 3a, where we plot the THz-range interminiband absorption spectrum of the structure of Figure 2 (again, with Fermi level fixed at the top of miniband V3), for different values of U_{SL} at T = 5 K. The frequency of maximum absorption ν_{peak}, indicated by the dotted line in the color map, can be varied across a wide portion of the THz spectrum with relatively small changes in SL potential. The progressive flattening of both minibands V2 and V3 with increasing U_{SL} also explains the observed saturation in ν_{peak} at large values of the SL potential. The accessible tuning range ($\nu_{peak} \leq 9.2$ THz in Figure 3a) can be increased using SLs of shorter period Λ (see Supporting Information, Figure S2), where the larger size of the MBZ allows for larger energy variations across each miniband at any given voltage.

By virtue of their large peak values, relatively steep edges, and broad tunability, the absorption spectra of the SL just described are particularly attractive for the development of THz modulators capable of providing high contrast ratios. To illustrate, Figure 3c shows the single-pass transmission $e^{-\alpha}$ of the same structure at different frequencies plotted as a function of U_{SL}. At frequencies above 3.7 THz, $e^{-\alpha}$ can be decreased by a factor of over 100× by varying the SL potential from 0 to a value on the order of 100 meV or less. At lower frequencies,

DOI: 10.1021/acsphotonics.8b00584
ACS Photonics 2018, 5, 3331−3337

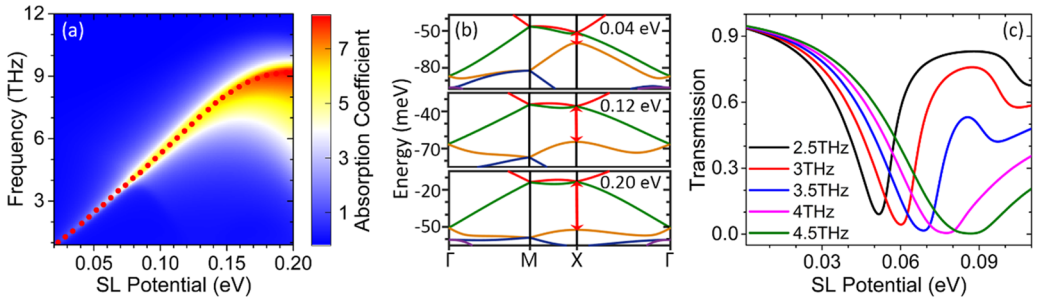

Figure 3. Dynamic tunability of interminiband absorption in graphene SLs. (a) Absorption spectra of the SL of Figure 2 at 5 K for different values of the potential U_{SL}. The dotted line indicates the frequency of peak absorption ν_{peak} as a function of U_{SL}. For each value of U_{SL}, the graphene Fermi level is fixed at the top of miniband V3. (b) Valence miniband structure of the same sample geometry for different values of U_{SL}. (c) Single-pass transmission $e^{-\alpha}$ of the same device at different frequencies plotted as a function of U_{SL}.

the maximum achievable contrast ratios are smaller, due to the proportionally smaller absorption peaks, but can be increased using SLs with larger period (see Supporting Information, Figure S2). The underlying modulation dynamics can also be expected to be ultrafast, since it depends on the external perturbation of an electronic band structure (e.g., similar to the quantum-confined Stark effect in semiconductor quantum wells[49]) and, thus, is not limited by any charge transport phenomena. The same interminiband transitions could also be employed for THz photodetection, even though they do not involve the direct generation of new electron−hole pairs. Instead, the energy of the absorbed light in these devices can be converted into heat and then detected through the photothermoelectric effect−a process that has already been shown to be quite efficient in the context of intraband THz absorption in plain graphene.[40] In this context, the narrowband nature and dynamic tunability of the interminiband transitions under study are also quite interesting as a way to enable novel functionalities, such as the development of extremely miniaturized THz spectrometers.

INTERMINIBAND GAIN

Next, we investigate THz light emission and amplification in the same graphene SLs. If the sample is undoped and a significant number of holes is then introduced in miniband V3 (e.g., by optical pumping or electrical injection), light emission peaked at the V2−V3 minigap frequency can be expected. The possibility of optical gain at the same frequency is enabled by the separation in reciprocal space between the absolute maxima of minibands V3 and V2, which are located at the X and M symmetry points of the MBZ, respectively (Figure 1d). In traditional SLs based on semiconductor quantum wells, when excess electrons (holes) are injected into a miniband, they tend to quickly relax into the available states near the minimum (maximum) of the same miniband, before eventually decaying into other minibands at lower (higher) energy.[6] The underlying intraminiband relaxation mechanism is primarily carrier−carrier scattering, which is particularly effective at equilibrating carriers among energetically adjacent states (as opposed to states separated by a finite energy gap). This general idea is exploited in SL quantum cascade lasers,[5−7] where a local population inversion is established between the extrema of two consecutive minibands even without a global inversion across the same two minibands. A detailed investigation of the corresponding intra- and interminiband carrier relaxation dynamics in graphene SLs has not been reported yet. However, a similar behavior as just described can be expected based on time-resolved studies with plain graphene.[50−53] In these reports, intraband equilibration by carrier−carrier scattering was found to occur on a much faster time scale compared to interband recombination (about 100 fs vs 1−10 ps at room temperature). As a result, separate quasi-Fermi distributions are established in different bands under nonequilibrium conditions. The associated carrier temperature dynamics (i.e., cooling to the lattice temperature via optical phonon emission) is more complex as it depends on the energy range of the initial hot-carrier distribution,[53] but generally takes place on an intermediate time scale.

With such relaxation dynamics in the SL of Figure 1, holes injected into minibands V3 and V2 will rapidly relax into states near their respective maxima at the X and M points, so that a local population inversion near X can be established. To estimate the resulting optical gain, we consider an optical pumping scheme where electrons and holes are introduced in an undoped SL through the absorption of externally incident light. The hole densities in minibands V2 and V3 (P_2 and P_3, respectively) are computed with a simple rate-equation model, similar to what is commonly used to study the threshold condition in quantum cascade lasers:[54]

$$\begin{cases} \dfrac{dP_3}{dt} = -\dfrac{P_3}{\tau_3} + r_3\Phi_p \\ \dfrac{dP_2}{dt} = \dfrac{P_3}{\tau_{32}} - \dfrac{P_2}{\tau_2} + r_2\Phi_p \end{cases} \tag{2}$$

In these equations, Φ_p is the photon flux of the pump light, r_n (for n = 2 or 3) is the fraction of incident pump photons that are absorbed through the creation of holes in miniband Vn, and τ_n is the lifetime of the corresponding miniband with $1/\tau_3 = 1/\tau_{32} + 1/\tau_{31}$ and $1/\tau_2 = 1/\tau_{21}$, where $1/\tau_{nm}$ is the hole interminiband decay rate from Vn to Vm. The hole densities P_2 and P_3 are obtained by solving eq 2 in steady state (i.e., with $d/dt \to 0$) and then used to evaluate the quasi-Fermi energies E_{F2} and E_{F3} of their respective minibands, again under the assumption of ultrafast intraminiband equilibration. Finally, the gain spectrum $g(\omega) = -\alpha(\omega)$ is computed from eq 1 with the occupation probabilities $f(E_n(\mathbf{k}))$ given by quasi-Fermi distribution functions with Fermi energies E_{Fn}.

In these calculations, the pump wavelength λ_p is selected so as to maximize r_3, while at the same time keeping r_2 as small as possible (see Supporting Information, Figure S3). Specifically, we use a resonance in the joint density of states of minibands V3 and C1 (illustrated by the dashed arrow in Figure 1d), which occurs at λ_p = 11.7 μm under the SL bias conditions of

DOI: 10.1021/acsphotonics.8b00584
ACS Photonics 2018, 5, 3331−3337

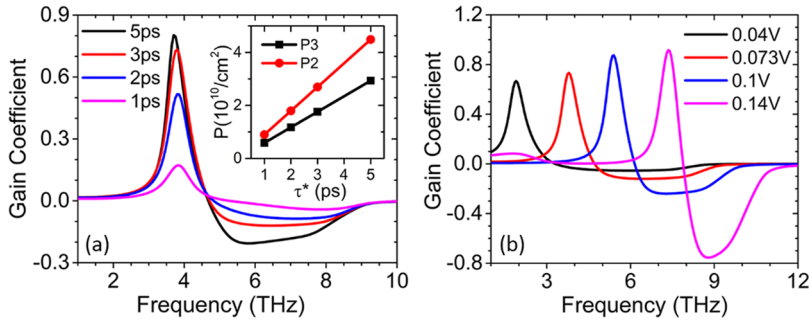

Figure 4. Interminiband gain in optically pumped graphene SLs. (a) Low-temperature gain spectrum of the SL of Figure 1 for different values of the interminiband relaxation lifetime τ^*. Inset: hole densities of minibands V2 and V3 vs τ^*. (b) Gain spectra of the same sample geometry for τ^* = 3 ps and different values of the SL potential U_{SL}.

Figure 1 (U_{SL} = 73 meV). The corresponding values of r_3 and r_2, evaluated using eq 1, are 10.7% and 2.6%, respectively. The photon flux Φ_p is computed for an input pump intensity (transmitted inside the graphene sheet) equivalent to 2 mW focused on a 10 × 10 μm^2 area. Finally, the scattering lifetimes τ_{nm} are taken to be in the picosecond range, in accordance with the experimental interband relaxation times of plain graphene.[50−53] For simplicity, we also introduce the assumption that these lifetimes are all equal to one another, that is, $\tau_{32} = \tau_{31} = \tau_{21} \equiv \tau^*$, and then study the gain-spectrum dependence on the single parameter τ^*. In fact, τ_{21} can be expected to be shorter than both τ_{32} and τ_{31}, given the close energetic proximity of minibands V2 and V1 along the M−X direction in the MBZ (Figure 1d), which favors fast hole interminiband relaxation from V2 to V1 by carrier−carrier scattering. Therefore, this assumption of equal interminiband decay rates can possibly lead to overestimating P_2 and thus underestimating the gain coefficient in the simulations below.

The interminiband gain spectrum of the SL of Figure 1 is shown in Figure 4a, computed for T = 5 K and different values of the time constant τ^* ranging from 1 to 5 ps. In these calculations, the broadening parameter δ of eq 1 is set equal to $1/\tau_{sc} + (1/\tau_2 + 1/\tau_3)/2$,[55] where the second term accounts for the additional interminiband scattering under the present nonequilibrium conditions. In each trace of Figure 4a, a sharp feature centered near the V2−V3 minigap frequency is obtained, with peak value as large as 0.8 for the longest time constant. If the same SL is placed inside a vertical optical cavity, the corresponding amplification factor per round trip e^{2g} is therefore nearly 5×. The inset shows the hole densities P_2 and P_3 computed in the same simulations. Regardless of the specific value of τ^*, the SL does not support a global population inversion between the minibands under study (i.e., P_3 is always smaller than P_2). The observed gain is then produced by the aforementioned local inversion near the X point of the MBZ, where miniband V2 is well below its maximum and therefore features smaller hole occupation probability (i.e., more electrons) than the maximum of V3 at the same point. Calculations based on the same model just presented with the same set of values for τ^* suggest that the presence of gain may be possible even at room temperature (see Supporting Information, Figure S4). However, more definitive predictions in this respect will require a deeper knowledge of the intra- and interminiband relaxation dynamics of graphene SLs than presently available.

The frequency of peak gain is also tunable with the SL potential U_{SL}, as illustrated in Figure 4b for τ^* = 3 ps. As already described above, increasing U_{SL} has the effect of flattening both minibands V2 and V3 near the X point and thus increase their energy separation, and as a result the gain spectrum is shifted to higher frequencies. The flattening of V3 throughout the MBZ at large values of U_{SL} (e.g., see bottom panel of Figure 3b) also causes a redistribution of its hole population across the entire miniband. Under these conditions, absorption of the pump light via transitions involving V3 can be partially saturated. This effect is not accounted for in the model of eqs 2, and its inclusion would require further assumptions about the SL intra- and interminiband relaxation dynamics. For this reason, in Figure 4b we only consider values of U_{SL} for which the hole occupation probability of the V3 states involved in the pumping transitions remains sufficiently small (<0.1%), so that absorption saturation of the pump light is not a concern. Similar to the case of the absorption spectra described above (see Supporting Information, Figure S2), the tuning range of the gain peak can also be extended using SLs of smaller period.

CONCLUSION

The simulation results presented in this work highlight the great potential of periodically gated graphene SLs for THz optoelectronic device applications. In particular, by virtue of their strong van Hove singularities in the joint density of states of select miniband pairs, these systems can provide narrowband absorption (or gain under suitable pumping), with giant peak values for 2D materials. These absorption and emission features are also broadly tunable (with relatively small changes in the SL potential), which represents a distinctive advantage over traditional THz optoelectronic materials. Specific device applications that can be envisioned include modulators with large contrast ratio and high speed, and narrowband tunable photodetectors. Furthermore, the ability of the same systems to provide interminiband gain may open the way for a new class of compact THz lasers inspired by prior work with quantum-well SLs.[5−7] The ultimate performance capabilities of such THz sources depend on the detailed intra- and interminiband carrier dynamics of graphene SLs, and the present work therefore provides a direct motivation for the investigation of these phenomena. It should also be noted that, while the simulations of Figure 4 have focused on optical pumping for simplicity, suitable electrical-injection schemes could also be devised, for example, based on tunneling from an adjacent graphene sheet across an intervening 2D insulator such as h-BN. Altogether, graphene SLs therefore represent a promising new materials platform to address a long-standing

DOI: 10.1021/acsphotonics.8b00584
ACS Photonics 2018, 5, 3331−3337

gap in optoelectronic science and technology, that is, the lack of high-performance solid-state THz devices.

■ ASSOCIATED CONTENT

Supporting Information

The Supporting Information is available free of charge on the ACS Publications website at DOI: 10.1021/acsphotonics.8b00584.

Additional simulation results showing interminiband absorption versus carrier scattering lifetime and SL period, optimization of the pump wavelength used in the gain calculations, and interminiband gain versus temperature (PDF).

■ AUTHOR INFORMATION

Corresponding Author

*E-mail: rpaiella@bu.edu.

ORCID

Roberto Paiella: 0000-0002-7183-6249

Notes

The authors declare no competing financial interest.

■ ACKNOWLEDGMENTS

This work was partly supported by the National Science Foundation under Grant No. DMR-1308659. Some of the simulations were performed using the Shared Computing Cluster facility at Boston University.

■ REFERENCES

(1) Esaki, L.; Tsu, R. Superlattice and Negative Differential Conductivity in Semiconductors. *IBM J. Res. Dev.* **1970**, *14*, 61−65.

(2) Tsu, R. *Superlattice to Nanoelectronics*; Elsevier: Amsterdam, 2005.

(3) Helm, M.; Hilber, W.; Fromherz, T.; Peeters, F. M.; Alavi, K.; Pathak, R. N. Infrared Absorption in Superlattices: A Probe of the Miniband Dispersion and the Structure of the Impurity Band. *Phys. Rev. B: Condens. Matter Mater. Phys.* **1993**, *48*, 1601−1606.

(4) Stehr, D.; Metzner, C.; Helm, M.; Roch, T.; Strasser, G. Resonant Impurity Bands in Semiconductor Superlattices. *Phys. Rev. Lett.* **2005**, *95*, 257401.

(5) Scamarcio, G.; Capasso, F.; Sirtori, C.; Faist, J.; Hutchinson, A. L.; Sivco, D. L.; Cho, A. Y. High-Power Infrared (8-Micrometer Wavelength) Superlattice Lasers. *Science* **1997**, *276*, 773−776.

(6) Capasso, F.; Tredicucci, A.; Gmachl, C.; Hutchinson, A. L.; Sivco, D. L.; Cho, A. Y. High Performance Quantum Cascade Lasers with Superlattice Active Regions. *IEEE J. Sel. Top. Quantum Electron.* **1999**, *5*, 792−807.

(7) Köhler, R.; Tredicucci, A.; Beltram, F.; Beere, H.; Linfield, E.; Davies, A.; Ritchie, D.; Iotti, R.; Rossi, F. Terahertz Semiconductor-Heterostructure Lasers. *Nature* **2002**, *417*, 156−159.

(8) Yankowitz, M.; Xue, J.; Cormode, D.; Sanchez-Yamagishi, J. D.; Watanabe, K.; Taniguchi, T.; Jarillo-Herrero, P.; Jacquod, P.; Leroy, B. J. Emergence of Superlattice Dirac Points in Graphene on Hexagonal Boron Nitride. *Nat. Phys.* **2012**, *8*, 382−386.

(9) Ponomarenko, L. A.; Gorbachev, R. V.; Yu, G. L.; Elias, D. C.; Jalil, R.; Patel, A. A.; Mishchenko, A.; Mayorov, A. S.; Woods, C. R.; Wallbank, J. R.; Mucha-Kruczynski, M.; Piot, B. A.; Potemski, M.; Grigorieva, I. V.; Novoselov, K. S.; Guinea, F.; Fal'ko, V. I.; Geim, A. K. Cloning of Dirac Fermions in Graphene Superlattices. *Nature* **2013**, *497*, 594−597.

(10) Dean, C. R.; Wang, L.; Maher, P.; Forsythe, C.; Ghahari, F.; Gao, Y.; Katoch, J.; Ishigami, M.; Moon, P.; Koshino, M.; Taniguchi, T.; Watanabe, K.; Shepard, K. L.; Hone, J.; Kim, P. Hofstadter's Butterfly and the Fractal Quantum Hall Effect in Moiré Superlattices. *Nature* **2013**, *497*, 598−602.

(11) Hunt, B.; Sanchez-Yamagishi, J. D.; Young, A. F.; Yankowitz, M.; Leroy, B. J.; Watanabe, K.; Taniguchi, T.; Moon, P.; Koshino, M.; Jarillo-Herrero, P.; Ashoori, R. C. Massive Dirac Fermions and Hofstadter Butterfly in a Van der Waals Heterostructure. *Science* **2013**, *340*, 1427−1430.

(12) Ni, G. X.; Wang, H.; Wu, J. S.; Fei, Z.; Goldflam, M. D.; Keilmann, F.; Özyilmaz, B.; Castro Neto, A. H.; Xie, X. M.; Fogler, M. M.; Basov, D. N. Plasmons in Graphene Moiré Superlattices. *Nat. Mater.* **2015**, *14*, 1217−1222.

(13) Lee, M.; Wallbank, J. R.; Gallagher, P.; Watanabe, K.; Taniguchi, T.; Falko, V. I.; Goldhaber-Gordon, D. Ballistic Miniband Conduction in a Graphene Superlattice. *Science* **2016**, *353*, 1526−1529.

(14) Sun, Z.; Pint, C. L.; Marcano, D. C.; Zhang, C.; Yao, J.; Ruan, G.; Yan, Z.; Zhu, Y.; Hauge, R. H.; Tour, J. M. Towards Hybrid Superlattices in Graphene. *Nat. Commun.* **2011**, *2*, 559.

(15) Dubey, S.; Singh, V.; Bhat, A. K.; Parikh, P.; Grover, S.; Sensarma, R.; Tripathi, V.; Sengupta, K.; Deshmukh, M. M. Tunable Superlattice in Graphene to Control the Number of Dirac Points. *Nano Lett.* **2013**, *13*, 3990−3995.

(16) Drienovsky, M.; Schrettenbrunner, F.-X.; Sandner, A.; Weiss, D.; Eroms, J.; Liu, M.-H.; Tkatschenko, F.; Richter, K. Towards Superlattices: Lateral Bipolar Multibarriers in Graphene. *Phys. Rev. B: Condens. Matter Mater. Phys.* **2014**, *89*, 115421.

(17) Forsythe, C.; Zhou, X.; Watanabe, K.; Taniguchi, T.; Pasupathy, A.; Moon, P.; Koshino, M.; Kim, P.; Dean, C. R. Band Structure Engineering of 2D Materials Using Patterned Dielectric Superlattices. *Nat. Nanotechnol.* **2018**, *13*, 566.

(18) Zhang, Y.; Kim, Y.; Gilbert, M. J.; Mason, N. Electronic Transport in a Two-Dimensional Superlattice Engineered via Self-Assembled Nanostructures. *arXiv: 1703.05689* **2017**, na.

(19) Park, C.-H.; Yang, L.; Son, Y.-W.; Cohen, M. L.; Louie, S. G. Anisotropic Behaviours of Massless Dirac Fermions in Graphene under Periodic Potentials. *Nat. Phys.* **2008**, *4*, 213−217.

(20) Barbier, M.; Vasilopoulos, P.; Peeters, F. M. Extra Dirac Points in the Energy Spectrum for Superlattices on Single-Layer Graphene. *Phys. Rev. B: Condens. Matter Mater. Phys.* **2010**, *81*, 75438.

(21) Wallbank, J. R.; Patel, A. A.; Mucha-Kruczyński, M.; Geim, A. K.; Falko, V. I. Generic Miniband Structure of Graphene on a Hexagonal Substrate. *Phys. Rev. B: Condens. Matter Mater. Phys.* **2013**, *87*, 245408.

(22) Moon, P.; Koshino, M. Electronic Properties of Graphene/Hexagonal-Boron-Nitride Moiré Superlattice. *Phys. Rev. B: Condens. Matter Mater. Phys.* **2014**, *90*, 155406.

(23) Shi, Z.; Jin, C.; Yang, W.; Ju, L.; Horng, J.; Lu, X.; Bechtel, H. A.; Martin, M. C.; Fu, D.; Wu, J.; Watanabe, K.; Taniguchi, T.; Zhang, Y.; Bai, X.; Wang, E.; Zhang, G.; Wang, F. Gate-Dependent Pseudospin Mixing in Graphene/Boron Nitride Moiré Superlattices. *Nat. Phys.* **2014**, *10*, 743−747.

(24) Wu, S.; Wang, L.; Lai, Y.; Shan, W.-Y.; Aivazian, G.; Zhang, X.; Taniguchi, T.; Watanabe, K.; Xiao, D.; Dean, C.; Hone, J.; Li, Z.; Xu, X. Multiple Hot-Carrier Collection in Photo-Excited Graphene Moiré Superlattices. *Science Adv.* **2016**, *2*, e1600002.

(25) Abergel, D. S. L.; Mucha-Kruczyński, M. Infrared Absorption of Closely Aligned Heterostructures of Monolayer and Bilayer Graphene with Hexagonal Boron Nitride. *Phys. Rev. B: Condens. Matter Mater. Phys.* **2015**, *92*, 115430.

(26) DaSilva, A. M.; Jung, J.; Adam, S.; MacDonald, A. H. Terahertz Conductivity of Graphene on Boron Nitride. *Phys. Rev. B: Condens. Matter Mater. Phys.* **2015**, *92*, 155406.

(27) Ryzhii, V.; Ryzhii, M.; Otsuji, T. Negative Dynamic Conductivity of Graphene with Optical Pumping. *J. Appl. Phys.* **2007**, *101*, 083114.

(28) Rana, F. Graphene Terahertz Plasmon Oscillators. *IEEE Trans. Nanotechnol.* **2008**, *7*, 91−99.

(29) Ju, L.; Geng, B.; Horng, J.; Girit, C.; Martin, M.; Hao, Z.; Bechtel, H. A.; Liang, X.; Zettl, A.; Shen, Y. R.; Wang, F. Graphene Plasmonics for Tunable Terahertz Metamaterials. *Nat. Nanotechnol.* **2011**, *6*, 630−634.

(30) Yan, H.; Li, X.; Chandra, B.; Tulevski, G.; Wu, Y.; Freitag, M.; Zhu, W.; Avouris, P.; Xia, F. Tunable Infrared Plasmonic Devices Using Graphene/Insulator Stacks. *Nat. Nanotechnol.* **2012**, *7*, 330−334.
(31) Boubanga-Tombet, S.; Chan, S.; Watanabe, T.; Satou, A.; Ryzhii, V.; Otsuji, T. Ultrafast Carrier Dynamics and Terahertz Emission in Optically Pumped Graphene at Room Temperature. *Phys. Rev. B: Condens. Matter Mater. Phys.* **2012**, *85*, 035443.
(32) Prechtel, L.; Song, L.; Schuh, D.; Ajayan, P.; Wegscheider, W.; Holleitner, A. W. Time-Resolved Ultrafast Photocurrents and Terahertz Generation in Freely Suspended Graphene. *Nat. Commun.* **2012**, *3*, 646.
(33) Sensale-Rodriguez, B.; Yan, R.; Kelly, M. M.; Fang, T.; Tahy, K.; Hwang, W. S.; Jena, D.; Liu, L.; Xing, H. G. Broadband Graphene Terahertz Modulators Enabled by Intraband Transitions. *Nat. Commun.* **2012**, *3*, 780.
(34) Ren, L.; Zhang, Q.; Yao, J.; Sun, Z.; Kaneko, R.; Yan, Z.; Nanot, S.; Jin, Z.; Kawayama, I.; Tonouchi, M.; Tour, J. M.; Kono, J. Terahertz and Infrared Spectroscopy of Gated Large-Area Graphene. *Nano Lett.* **2012**, *12*, 3711−3715.
(35) Vicarelli, L.; Vitiello, M. S.; Coquillat, D.; Lombardo, A.; Ferrari, A. C.; Knap, W.; Polini, M.; Pellegrini, V.; Tredicucci, A. Graphene Field-Effect Transistors as Room-Temperature Terahertz Detectors. *Nat. Mater.* **2012**, *11*, 865−871.
(36) Weis, P.; Garcia-Pomar, J. L.; Höh, M.; Reinhard, B.; Brodyanski, A.; Rahm, M. Spectrally Wide-Band Terahertz Wave Modulator Based on Optically Tuned Graphene. *ACS Nano* **2012**, *6*, 9118−9124.
(37) Sensale-Rodriguez, B. Graphene-Insulator-Graphene Active Plasmonic Terahertz Devices. *Appl. Phys. Lett.* **2013**, *103*, 123109.
(38) Tantiwanichapan, K.; Wang, X.; Swan, A. K.; Paiella, R. Graphene on Nanoscale Gratings for the Generation of Terahertz Smith-Purcell Radiation. *Appl. Phys. Lett.* **2014**, *105*, 241102.
(39) Yao, X.; Tokman, M.; Belyanin, A. Efficient Nonlinear Generation of THz Plasmons in Graphene and Topological Insulators. *Phys. Rev. Lett.* **2014**, *112*, 055501.
(40) Cai, X.; Sushkov, A. B.; Suess, R. J.; Jadidi, M. M.; Jenkins, G. S.; Nyakiti, L. O.; Myers-Ward, R. L.; Li, S.; Yan, J.; Gaskill, D. K.; Murphy, T. E.; Drew, H. D.; Fuhrer, M. S. Sensitive Room-Temperature Terahertz Detection via the Photothermoelectric Effect in Graphene. *Nat. Nanotechnol.* **2014**, *9*, 814−819.
(41) Tong, J.; Muthee, M.; Chen, S.-Y.; Yngvesson, S. K.; Yan, J. Antenna Enhanced Graphene THz Emitter and Detector. *Nano Lett.* **2015**, *15*, 5295−5301.
(42) Yadav, D.; Boubanga Tombet, S.; Watanabe, T.; Arnold, S.; Ryzhii, V.; Otsuji, T. Terahertz Wave Generation and Detection in Double-Graphene Layered Van der Waals Heterostructures. *2D Mater.* **2016**, *3*, 045009.
(43) Mittendorff, M.; Li, S.; Murphy, T. E. Graphene-Based Waveguide-Integrated Terahertz Modulator. *ACS Photonics* **2017**, *4*, 316−321.
(44) Wang, L.; Meric, I.; Huang, P. Y.; Gao, Q.; Gao, Y.; Tran, H.; Taniguchi, T.; Watanabe, K.; Campos, L. M.; Muller, D. A.; Guo, J.; Kim, P.; Hone, J.; Shepard, K. L.; Dean, C. R. One-Dimensional Electrical Contact to a Two-Dimensional Material. *Science* **2013**, *342*, 614−617.
(45) Gao, W.; Shi, G.; Jin, Z.; Shu, J.; Zhang, Q.; Vajtai, R.; Ajayan, P. M.; Kono, J.; Xu, Q. Excitation and Active Control of Propagating Surface Plasmon Polaritons in Graphene. *Nano Lett.* **2013**, *13*, 3698−3702.
(46) Tantiwanichapan, K.; Wang, X.; Durmaz, H.; Li, Y.; Swan, A. K.; Paiella, R. Graphene Terahertz Plasmons: a Combined Transmission Spectroscopy and Raman Microscopy Study. *ACS Photonics* **2017**, *4*, 2011−2017.
(47) Katsnelson, M. I. *Graphene: Carbon in Two Dimensions*; Cambridge University Press: New York, 2012; pp 161−184.
(48) Yan, H.; Xia, F.; Zhu, W.; Freitag, M.; Dimitrakopoulos, C.; Bol, A. A.; Tulevski, G.; Avouris, P. Infrared Spectroscopy of Wafer-Scale Graphene. *ACS Nano* **2011**, *5*, 9854−9860.
(49) Chemla, D. S.; Damen, T. C.; Miller, D. A. B.; Gossard, A. C.; Wiegmann, W. Electroabsorption by Stark Effect on Room-Temperature Excitons in GaAs/GaAlAs Multiple Quantum Well Structures. *Appl. Phys. Lett.* **1983**, *42*, 864−866.
(50) George, P. A.; Strait, J.; Dawlaty, J.; Shivaraman, S.; Chandrashekhar, M.; Rana, F.; Spencer, M. G. Ultrafast Optical-Pump Terahertz-Probe Spectroscopy of the Carrier Relaxation and Recombination Dynamics in Epitaxial Graphene. *Nano Lett.* **2008**, *8*, 4248−4251.
(51) Rana, F.; George, P. A.; Strait, J. H.; Dawlaty, J.; Shivaraman, S.; Chandrashekhar, M.; Spencer, M. G. Carrier Recombination and Generation Rates for Intravalley and Intervalley Phonon Scattering in Graphene. *Phys. Rev. B: Condens. Matter Mater. Phys.* **2009**, *79*, 115447.
(52) Breusing, M.; Kuehn, S.; Winzer, T.; Malić, E.; Milde, F.; Severin, N.; Rabe, J. P.; Ropers, C.; Knorr, A.; Elsaesser, T. Ultrafast Nonequilibrium Carrier Dynamics in a Single Graphene Layer. *Phys. Rev. B: Condens. Matter Mater. Phys.* **2011**, *83*, 153410.
(53) Winnerl, S.; Orlita, M.; Plochocka, P.; Kossacki, P.; Potemski, M.; Winzer, T.; Malic, E.; Knorr, A.; Sprinkle, M.; Berger, C.; de Heer, W. A.; Schneider, H.; Helm, M. Carrier Relaxation in Epitaxial Graphene Photoexcited Near the Dirac Point. *Phys. Rev. Lett.* **2011**, *107*, 237401.
(54) Paiella, R. Quantum Cascade Lasers. In *Comprehensive Semiconductor Science and Technology*; Bhattacharya, P., Fornari, R., Kamimura, H., Eds.; Elsevier, 2011; Vol. *5*, pp 683−723.
(55) Saleh, B. E. A.; Teich, M. C. *Fundamentals of Photonics*; John Wiley & Sons, 2007; pp 511−515.

DOI: 10.1021/acsphotonics.8b00584
ACS Photonics 2018, 5, 3331−3337